

# Moho Inversion by Gravity Anomalies in the South China Sea: Updates and Improved Iteration of the Parker-Oldenburg Algorithm.

Weibo Rao<sup>1</sup>, Nan Yu<sup>2</sup>, Gang Chen<sup>3</sup>, Xinyu Xu<sup>4</sup>, Simin Zhao<sup>4</sup>, Zhaoqi Song<sup>1</sup>, Jiazheng Liu<sup>1</sup>, Longtu Wan<sup>1</sup>, and Changhong Hu<sup>5</sup>

<sup>1</sup>College of Marine Science and Technology, China University of Geosciences, Wuhan, China

<sup>2</sup>College of Marine Science and Technology, China University of Geosciences, Wuhan, China; Hubei Key Laboratory of Marine Geological Resources, China University of Geosciences, Wuhan, China

<sup>3</sup>College of Marine Science and Technology

<sup>4</sup>School of Geodesy and Geomatics, Wuhan University, Wuhan 430079, China

<sup>5</sup>College of Marine Science and Technology, China University of Geosciences, Wuhan, China Edit Remove

December 15, 2022

## Abstract

The Moho is the interface between crust and mantle, and accurate location of the Moho is important for both resource exploration and deep earth condition and structural change investigations. The Parker-Oldenburg (P-O) method, is simple and efficient and thus has been extensively applied in the frequency domain and for Moho depth inversion. However, Moho fluctuation simulations using the P-O method are not reliable because of the lack of field geographic data constraints during the inversion process and excessively smoothing of data details caused by using a filter to correct the source data signals. To solve those problems, we propose an improved iteration P-O method with variable density, the iterative process is constrained by geological data in the inversion parameters, and the variable depth of the gravity interface is iterated using an equivalent form of upward continuation in the Fourier domain, which is more stable and convergent than downward continuation term in original P-O method. Synthetic experiments indicate that improved method has the better consistency among the simulations than original method, and our improved method has the smallest RMS of 0.59 km. In a real case, we employed the improved method to invert the Moho depth of the South China Sea, and the RMS between our Moho model and the seismological data is the smallest value of 3.87 km. The synthetic experiments and application of the model to the SCS further prove that our method is practical and efficient.

## Hosted file

952006\_0\_art\_file\_10528876\_rms736.docx available at <https://authorea.com/users/566496/articles/613171-moho-inversion-by-gravity-anomalies-in-the-south-china-sea-updates-and-improved-iteration-of-the-parker-oldenburg-algorithm>

1  
2 **Moho Inversion by Gravity Anomalies in the South China Sea: Updates and**  
3 **Improved Iteration of the Parker-Oldenburg Algorithm.**

4 **Weibo Rao<sup>1,2</sup>, Nan Yu<sup>1,2,3,\*</sup>, Gang Chen<sup>2,\*</sup>, Xinyu Xu<sup>4</sup>, Simin Zhao<sup>4</sup>, Zhaoqi Song<sup>2</sup>,**  
5 **Jiazheng Liu<sup>2</sup>, Longtu Wan<sup>2</sup>, and Changhong Hu<sup>2</sup>**

6 <sup>1</sup> Hubei LuoJia Laboratory, Wuhan 430079, China.

7 <sup>2</sup> College of Marine Science and Technology, China University of Geosciences, Wuhan 430074,  
8 China.

9 <sup>3</sup> Wuhan Gravitation and Solid Earth Tides National Observation and Research Station, Wuhan  
10 430071, China.

11 <sup>4</sup> School of Geodesy and Geomatics, Wuhan University, Wuhan 430079, China

12 Corresponding author: Nan Yu ([yunan@cug.edu.cn](mailto:yunan@cug.edu.cn)) Gang Chen([ddwhcg@cug.edu.cn](mailto:ddwhcg@cug.edu.cn))

13 **Key Points:**

- 14 • An improved method uses an equivalent form of upward continuation in the Fourier  
15 domain and does no filter the iteration.
- 16 • Gravity inversion combines the actual density variations between layers.
- 17 • Moho inversion in the South China Sea fits well with the seismic Data, and our Moho  
18 depths model have the smallest RMS (3.87km).
- 19

## 20 Abstract

21 The Moho is the interface between crust and mantle, and accurate location of the Moho is  
22 important for both resource exploration and deep earth condition and structural change  
23 investigations. The Parker-Oldenburg (P-O) method, is simple and efficient and thus has been  
24 extensively applied in the frequency domain and for Moho depth inversion. However, Moho  
25 fluctuation simulations using the P-O method are not reliable because of the lack of field  
26 geographic data constraints during the inversion process and excessively smoothing of data  
27 details caused by using a filter to correct the source data signals. To solve those problems, we  
28 propose an improved iteration P-O method with variable density, the iterative process is  
29 constrained by geological data in the inversion parameters, and the variable depth of the gravity  
30 interface is iterated using an equivalent form of upward continuation in the Fourier domain,  
31 which is more stable and convergent than downward continuation term in original P-O method.  
32 Synthetic experiments indicate that improved method has the better consistency among the  
33 simulations than original method, and our improved method has the smallest RMS of 0.59 km. In  
34 a real case, we employed the improved method to invert the Moho depth of the South China Sea,  
35 and the RMS between our Moho model and the seismological data is the smallest value of 3.87  
36 km. The synthetic experiments and application of the model to the SCS further prove that our  
37 method is practical and efficient.

## 38 1 Introduction

39 The exploration and inversion of the internal structure of the Earth's layers is important for  
40 understanding geological conditions and structural changes. Seismic waves are the most direct  
41 and traditional method for studying the internal structure of the deep earth, and they have been  
42 used for seismic reflection (Agius & Lebedev, 2014; Q. Wang et al., 2016), deep seismic  
43 sounding profiles(Teng et al., 2013; X. Wang et al., 2017), receiver function analysis, and  
44 seismic tomography(Koulakov et al., 2015; Obrebski et al., 2012). However, conducting seismic  
45 detection is difficult in extreme geographical areas, such as mountains, oceans, and polar  
46 regions. In those dangerous regions where seismic data are sparse or missing, using global  
47 coverage high-resolution satellite gravity data can mitigate these limitations partially(W. Chen &  
48 Tenzer, 2017). Therefore, using high-resolution satellite gravity data to derive subsurface  
49 structure has become a new and practical method for field detection.

50 The Mohorovičić discontinuity (Moho) marks the transition from crust to mantle, whose  
51 fluctuation or depth variations are studied almost exclusively through indirect geophysical  
52 methods, including seismology and gravimetry, Moho is closely related to regional tectonics and  
53 oil-bearing structures. As various observation methods have improved, the accuracy of gravity  
54 data has reached a high level, which makes it possible to derive crustal models at both regional  
55 and global scale(Drinkwater et al., 2003; Reigber et al., 2002; Tapley et al., 2004). Earth gravity  
56 field models of high-resolution constructed based on satellite observations, as EGM2008,  
57 GOCO06s, and Tongji-Grace02s, can provide almost homogeneous data coverage, even in  
58 extremely harsh areas that are inaccessible to humans(Q. Chen et al., 2018; Kvas et al., 2021;  
59 Pavlis et al., 2012).

60 A nonlinear inverse problem during the process of Moho depth estimation using gravity  
61 data. To solve this problem, a series of methods has been developed over the years. Bott  
62 proposed a fast iterative algorithm by applying corrections to a starting estimate based on  
63 inversion residuals, and it can bypass the construction and solution of linear systems and only

64 involves forward modelling (Bott, 1960). Parker introduced an efficient 2-D and 3-D complexly  
65 layered model that can be directly applied to the evaluation of gravity effects on terrain relief or  
66 sediment layers(Parker, 1973). Oldenburg provided useful iterative procedures by rearranging  
67 Parker's formula, and this method is conducive to the inversion of either shape of the layer with  
68 known physical properties(Oldenburg, 1974). Sjöberg used the isostasy approach to solve the  
69 Vening Meinesz-Moritz inverse problem(Bagherbandi, 2012; Sjöberg, 2009, 2013). Parker-  
70 Oldenburg has become the most popular and reliable method in the field of crust (Moho)  
71 interface inversion by gravity field observations (M. Chen et al., 2018; DU et al., 2022;  
72 Grigoriadis et al., 2016; HE et al., 2019; H. LI et al., 2020).

73 Many improvements have been made to the original Parker-Oldenburg (P-O) method.  
74 Granser simplified the P-O algorithm by introducing Bott's iterative procedure to the original  
75 method, which is useful and mathematically less sophisticated (Granser, 1987; Xia & Sprowl,  
76 1995; H. Zeng et al., 1997). Several studies have enhanced the efficiency and effectiveness by  
77 improving the iteration procedures of the P-O method (XIAO et al., 2007; XU, 2006; C. Zhang et  
78 al., 2015). Some studies have focused on the engineering application of the P-O method, which  
79 extended its applicability and practicability (Gómez-Ortiz & Agarwal, 2005; Nagendra et al.,  
80 1996; Shin et al., 2006). In addition, the density model used in the P-O method is horizontally  
81 variable but vertically constant because of compositional differences in the crust and mantle, that  
82 lead to variations in the density model in the lateral direction. The P-O method has been  
83 extended by many scientists to several vertically variable density models, such as exponential  
84 (Chappell & Kusznir, 2008; R. Feng et al., 1986; Granser, 1987; ZHANG et al., 2020), parabolic  
85 (Shi et al., 2015; E.-H. ZHANG et al., 2015; ZHANG et al., 2020) , and general polynomial  
86 models (Chai & Jia, 1990; Guspi, 1992).

87 The application of the fast Fourier transform method (FFT) has accelerated the calculation  
88 process for the P-O iteration. The iteration is also convergent because of the involvement of a  
89 downward continuation operator using a low-pass filter. However, the FFT also reduce the  
90 accuracy of the P-O method substantially because of the inherent defects of FFT(i.e., aliasing,  
91 edge effects, imposed periodicity, and truncation effect) (Zhao et al., 2018). In this study, we  
92 present an improved iterarion P-O method with variable density. First, in the iteration procedures  
93 of our method, we improve the caculation and provide an approach to downward continuation  
94 using upward continuation iteration, and our method can obtain a more accurate and convergent  
95 inversion than those obtained from the general amplification factor suppression technology.  
96 Second, based on the constraints of gravity data and geological information in the survey area,  
97 the inversion with variable density by the improved method corresponds better with real  
98 geological conditions.

## 99 **2 Materials and Methods**

### 100 **2.1 Original Parker-Oldenburg method**

101 Parker derived a fast gravity forward modeling based on FFT (Parker, 1973), which can  
102 calculate the potential anomaly caused by different underground interfaces in the frequency  
103 domain. The Fourier transform of gravity anomaly is caused by an uneven layer; therefore,a  
104 uniform layer can be calculated as follows:

$$F[\Delta g] = -2\pi G \rho e^{(-|\vec{k}|h_0)} \sum_{n=1}^{\infty} \frac{|\vec{k}|^{n-1}}{n!} F[h^n(\vec{r})] \quad (1)$$

Where  $F[ ]$  denotes the Fourier transform operator;  $\Delta g$  is the gravity anomaly,  $G$  means the gravitational constant,  $\rho$  is the density contrast across the interface, i.e. ( $\rho = \rho_{below} - \rho_{above}$ ),  $|\vec{k}|$  is the wavenumber, that shows the magnitude of the wavenumber;  $h_0$  is the mean depth of the interface, and  $h(\vec{r})$  represents the variation from the mean depth of the interface, the axis system has  $z$  vertically downward with  $z_0 > 0$ .

Oldenburg rearranged the method of Parker (formula (1)), transposed the  $n=1$  term from the infinite sum, and finally obtained a formula to calculate the depth of the interface in the frequency domain (Oldenburg, 1974):

$$h(\vec{r}) = -F^{-1} \left[ \frac{F[\Delta g] e^{(|\vec{k}|h_0)}}{2\pi G \rho} + \sum_{n=2}^{\infty} \frac{|\vec{k}|^{n-1}}{n!} F[h(\vec{r})^n] \right] \quad (2)$$

The fluctuation of the different density interfaces underground can be calculated by formula (2), while in the frequency domain, the exponential amplification factors will also magnify the errors and even reduce the precision, which will then cause the divergence of the inversion, especially in high-frequency signals. A series of studies have proposed different solutions to ensure the convergence of inversions: Oldenburg kept convergence of formula (2) by using low-pass filters (Oldenburg, 1974); Guan calculated the depth of different domains to avoid the divergence of inversion (Guan, 1991); and Ahmed replaced the Fourier transform with the cosine transform in the algorithm (Ahmed et al., 1974). Overall, such optimizations of the P-O method are collectively referred to as classical gravity inversions. However, the above methods may select the wrong filter, and cause the loss of useful information, which will lead the interface of the inversion to deviate from the real situation. To solve this problem, we derived an improved iterative algorithm for the P-O method, which was iterated using an equivalent form of upward continuation in the Fourier domain. This improved method is more stable and convergent than the downward continuation term in the original method does not require filters.

## 2.2 Improved iteration P-O method with variable density

Xu presented a potential field continuation method that based on integral and iterative calculations (XU, 2006), Xiao proposed the idea that Xu's method could be used to probe Earth's interior (XIAO et al., 2007), Zhang completed Xiao's research and obtained an algorithm that does not require high-frequency filtering during iteration (C. Zhang et al., 2015). These improvements to the iteration are based on the original P-O method, and it is assumed that the original P-O method calculated based on a constant density contrast model, although this scenario is much more complicated in real cases. Ke proposed a variable density forward modelling based on the original method, and the results correspond well with the reality in the Tibetan Plateau (KE et al., 2006). Zhou developed the vector-potential line-integral method, which varies simply in one direction and complexly in three directions, and it can calculate the gravity anomaly resulting from a rectangular prism with density contrast (Zhou, 2009). Based on previous studies, we propose an improved gravity inversion method that combines the

142 advantages of the calculation process with the improved iteration and detailed variable density  
 143 model.

144 In order to introduce variable density parameters, the relationship between density and  
 145 depth can be fitted by an exponential function:

$$146 \quad \rho(r) = \rho_0 e^{-\mu h} \quad (3)$$

147 where  $\rho_0$  is the residual density of the surface geological medium,  $\mu$  is the attenuation  
 148 coefficient of density with depth change,  $h$  is the depth, thus, so  $\rho(r)$  is the variable density  
 149 function. In the frequency domain, the gravity forward algorithm constrained by exponential  
 150 variable density models is(ZHANG & MENG, 2013):

$$151 \quad F[\Delta g] = -2\pi G e^{(-|\bar{k}|h_0)} \sum_{n=1}^{\infty} \frac{|\bar{k} - \mu|^{n-1}}{n!} F[\rho(r) h^n(\bar{r})] \quad (4)$$

152 Taking the gravitational field into example, the nonconvergent term  $e^{|\bar{k}|h_0}$  in the Parker-  
 153 Oldenburg method (formula (2)) is equivalent to the Fourier transformation factor of downward  
 154 continuation, in terms of this aspect, upward continuation of the Fourier transformation is:

$$155 \quad F[\Delta g(x, y, -z_0)] = F[\Delta g(x, y, 0)] \cdot e^{(-z_0|\bar{k}|)} \quad (5)$$

156 In the formula,  $z_0$  is the vertical coordinate after downward continuation and  $z_0 > 0$ . By  
 157 analogy, Zhang's exponential variable density model (formula (4)) can be arranged into the same  
 158 form as formula (5):

$$159 \quad F[\Delta g] = F \left[ -2\pi G \sum_{n=1}^{\infty} \frac{|\bar{k} - \mu|^{n-1}}{n!} \rho(r) h^n(\bar{r}) \right] e^{(-|\bar{k}|h_0)} \quad (6)$$

160 The upward continuation formula (5) and Zhang's model (formula (6)) is similar. Here, we  
 161 improve the inversion of Xiao and Zhang. The derivation process of the improved method is  
 162 listed as follows:

163 <i> The forms of formula (5) and formula (6) are similar, which inspire us to explore the  
 164 connection of those formulas. We find that Zhang's model can be formally reflected as the  
 165 upward continuation of gravity anomaly in Xu's theory, let  $\Delta g(x, y, z) = \Delta g(x, y, 0)$ , and  
 166 formula (6) is:

$$167 \quad \Delta g = -2\pi G \sum_{n=1}^{\infty} \frac{|\bar{k} - \mu|^{n-1}}{n!} \rho(r) h^n(\bar{r}) \quad (7)$$

168 <ii>Combine formula (6) with the upward continuation formula (5) after reforming, then we  
 169 can obtain formula (6) as follow:

$$170 \quad \Delta g(x, y, z)^{(1)} = F^{-1} \left[ F \left[ -2\pi G \sum_{n=1}^{\infty} \frac{|\bar{k} - \mu|^{n-1}}{n!} \rho(r) h^{(1)}(\bar{r})^n \right] \cdot e^{(-h_0|\bar{k}|)} \right] \quad (8)$$

171 <iii> In Xu's theory, there is a method for potential field continuation using integral and  
 172 iterative calculation. Given two potential surfaces  $u_B$  and  $u_A$ , the upper known field  $u_B$  can  
 173 downward continue the unknown field  $u_A$ , a brief description is as follows:

$$174 \quad u_A^{(n+1)} = u_A^{(n)} + s(u_B - u_B^{(n)}) \quad (9)$$

175 where  $s$  is the step of iteration that is related to the number of iterations, and generally  $0 \leq s \leq 1$  ;  
 176 and  $\varepsilon$  is a minimum. When  $|u_B - u_B^{(n)}| < \varepsilon$  , it can be considered that  $u_A^{(n+1)} \approx u_A^{(n)}$  , and the  
 177 accuracy of iterative inversion is appropriate. In the improved iteration of P-O inversion,  $u_A$   
 178 means  $\Delta g(x, y, z)$  ,  $u_B$  means  $\Delta g(x, y, 0)$  .

179 <iv>The difference between the truth value  $\Delta g$  and the iterated value  $\Delta g^{(n)}$  is used to  
 180 correct the inversion, one obtains that  
 181  $\Delta g(x, y, z)^{(n+1)} = \Delta g(x, y, z)^{(n)} + s(\Delta g(x, y, 0) - \Delta g(x, y, 0)^{(n)})$  , and the improved iterative  
 182 inversion formula is finally obtained:

$$183 \quad -2\pi G \sum_{n=1}^{\infty} \frac{|\bar{k} - \mu|^{n-1}}{n!} \rho(r) h^{(n+1)}(\vec{r})^n = -2\pi G \sum_{n=1}^{\infty} \frac{|\bar{k} - \mu|^{n-1}}{n!} \rho(r) h^{(n)}(\vec{r})^n + s \left( g_z - F^{-1} \left[ F \left[ -2\pi G \sum_{n=1}^{\infty} \frac{|\bar{k} - \mu|^{n-1}}{n!} \rho(r) h^{(1)}(\vec{r})^n \cdot e^{(-h_0|\bar{k}|)} \right] \right] \right)$$

$$184 \quad (10)$$

185 similarly,  $s$  is the step of iteration ( $0 \leq s \leq 1$ ),  $\varepsilon$  is a minimum. When  $|\Delta g - \Delta g^{(n)}| < \varepsilon$  , the  
 186 inversion meets the criteria for convergence of iteration.

187 <v>The term on the right-hand can be considered that  $h^{(n+1)}(\vec{r}) \approx h^{(n)}(\vec{r})$  , and the depth of  
 188 the Moho is  $Depth = h_0 + h^{(n)}(\vec{r})$  . With the above deductions, the final summarized expression  
 189 like that:

$$190 \quad h^{(n+1)}(\vec{r}) = h^{(n)}(\vec{r}) + \frac{1}{-2\pi G \rho_0 e^{-\mu h}} \cdot s \left( \Delta g - F^{-1} \left[ F \left[ -2\pi G \sum_{n=1}^{\infty} \frac{|\bar{k} - \mu|^{n-1}}{n!} \rho(r) h^{(1)}(\vec{r})^n \cdot e^{(-h_0|\bar{k}|)} \right] \right] \right)$$

$$191 \quad (11)$$

192 Combining all the steps presented above, the whole iteration procedure of the improved  
 193 algorithm is summarized as a flow chart in Figure 1.

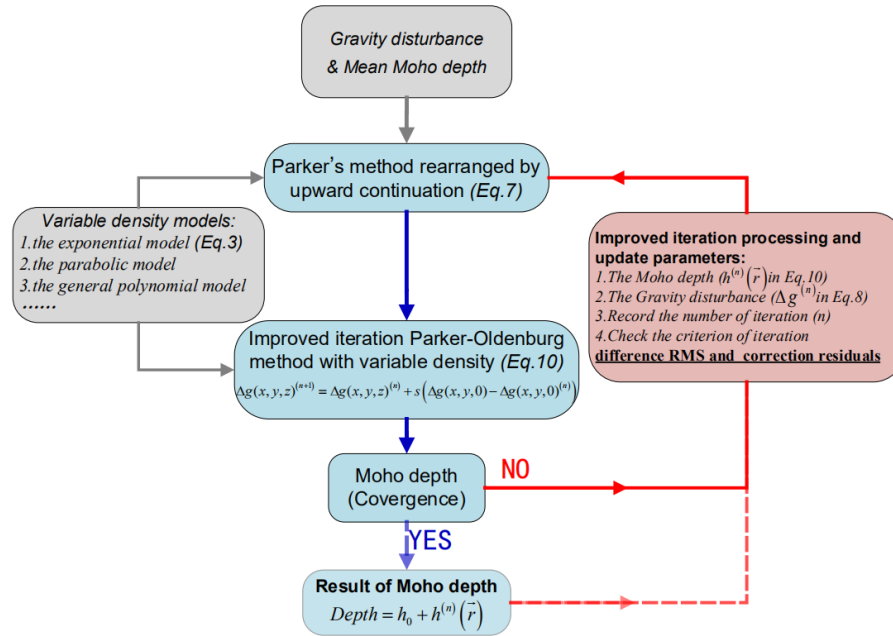


**Figure 1. Flow chart of our improved algorithm.**

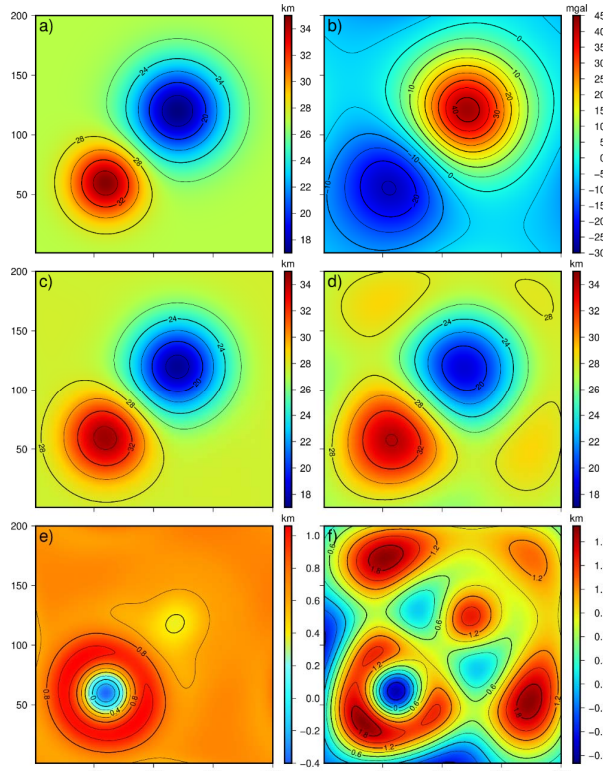
As shown in Figure 1, the specific use of equations in the improved inversion procedure are emphasized and processes that need to be executed iteratively are updated. The data source (listed in the top grey block) in the inversion contains two parts: gravity anomaly data and the average depth of the Moho surface in the study area. The variable density contrast model (listed in the left grey block) involved in the inversion includes exponential, parabolic, and general polynomial models. The red block on the right shows the data update during the iteration of the algorithm and the completion time of the iteration. The blue blocks in the middle column are the core of the entire algorithm, illustrating the intermediate calculations of the iteration and the equations used in the algorithm. In addition, the convergence verification of the upward continuation in the algorithm has been deduced in previous studies (Luo & Wu, 2016; X. N. Zeng et al., 2013).

Compared with the original Parker-Oldenburg algorithm (J. FENG et al., 2014; Gao & Sun, 2019; Qin et al., 2021; ZHANG et al., 2020), our method avoids the exponential amplification factor ( $e^{|\bar{k}|h_0}$ ) in the frequency domain, retains the details of the data; moreover, because of the introduction of variable density contrasts ( $\rho(r) = \rho_0 e^{-\mu h}$ ), which are obtained from the field, the inversion results correspond quite well with the topographic observations.

### 3 Numerical Experiments

To verify the effect of the improved iteration inversion (formula (11)) and original P-O methods (formula (2)), numerical experiments were performed under the same conditions. We designed a synthetic underground interface with a mean depth of 27 km and extension of 200 km×200 km (Figure 2 a)). We set a simulation experiment range of 200×200 columns and rows, which were separated by 1km. Two different fluctuations were included in the simulation experiment, and the observation plane was at  $z = 0$ . The horizontal center position of the dome was located at (60, 60), with a radius of 30 km and a maximum depth of 8km from the mean interface. The horizontal center positions of the basin were located at (120, 120), with a radius of 40 km and a maximum depth is -10km from the mean interface. The density contrast parameter of the

222 interface was constant  $0.29 \text{ g/cm}^3$ .



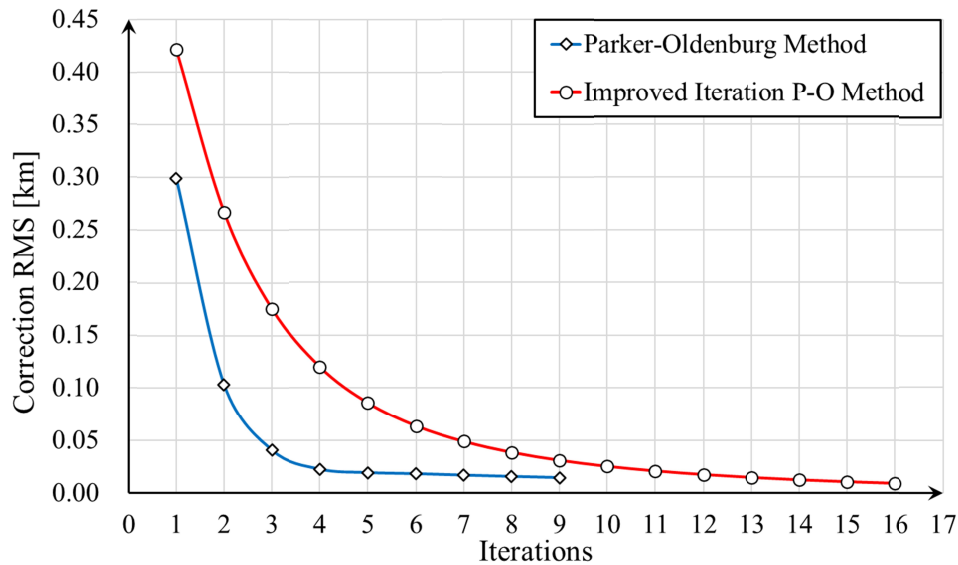
223  
224 **Figure 2. a) The geometry of synthetic underground interface. b) Gravity anomaly of the**  
225 **interface by Parker’s forward modeling. c) Inversion calculated by our improved iteration**  
226 **method with constant density. d) Inversion calculated by the original P-O method. e)**  
227 **Difference between Figure 2 a) and Figure 2 c). f) Difference between Figure 2 a) and**  
228 **Figure 2 d).**

229 Figure 2 b) shows the theoretical gravity anomaly induced by the Parker's forward modeling  
230 (formula (1)), which represents the input data of two inversion methods. Figure 2 d) shows the  
231 interface inverted by the improved iteration inversion from the input data, the gravity anomaly  
232 calculated from the formula (1). The average depth of inversion is 27km, the highest point is at  
233 (59,59) with a height of 34.51km, and the lowest point of depression is at (120,120) with a height  
234 of 17.38km. The iterate number of calculation is 16, the time required for calculation is 1.53s  
235 (containing the forward calculation time), and the total RMS (root mean square) compared with  
236 the simulation is 0.59km. A comparison between the results (Figure 2 c)) and the simulation  
237 (Figure 2 a)) is shown in Figure 2 e). Figure 2 d) shows the interface inverted from the gravity  
238 anomaly by the P-O method, and the parameters of low-pass filters (WH and SH) are chosen by  
239 multiple spectrum analysis so that we can get the optimal outcome of P-O method. The average  
240 depth of the inversion is 27.18km, the highest point of the relief is at (58,58), with a height of  
241 34.09km, and the lowest point of the depression is at (119,119) with a height of 18.54km. The  
242 iterate number of calculation is 9, the consuming time of calculations is 0.86 s ,and the total RMS  
243 is 0.66 km compared with the simulation. A comparison between Figure 2 d) and the simulation  
244 in Figure 2 a) is shown in Figure 2 f), and brief effect comparisons are listed in Table 1.

245 **Table 1. The comparison of two methods in numerical experiments with constant density**

Test Groups	Contrast ( $\text{g/cm}^3$ )	Highest (km)	Lowest (km)	Criterion	Iterations	Time (s)	RMS
Simulation	0.29	(60,60,35)	(120,120,17)	Null	Null	0	0

Parker-Oldenburg method	0.29	(58,58,34.09)	(119,119,18.54)	0.01	9	0.86	0.66
Improved Iteration P-O method	0.29	(59,59,34.51)	(120,120,17.38)	0.01	16	1.53	0.59

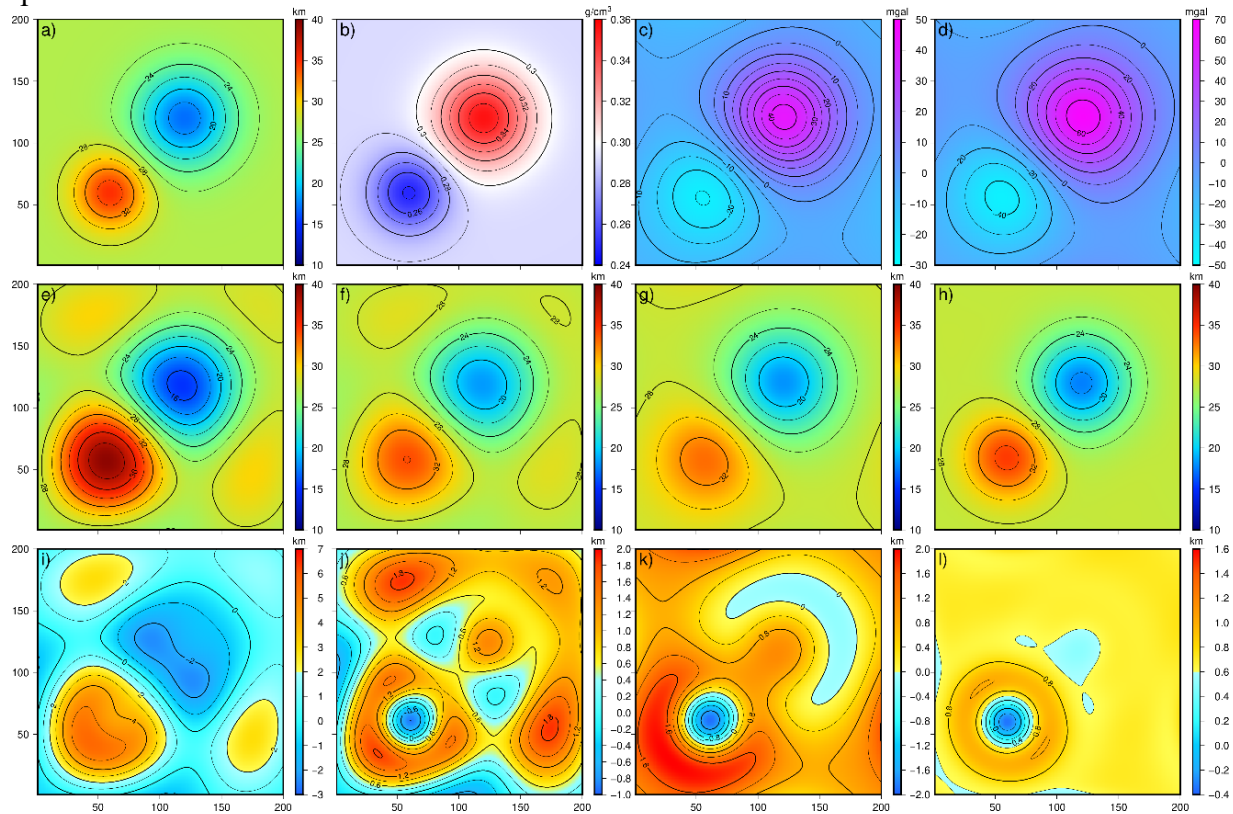


246  
247 **Figure 3. Statistics of the correction RMS, including Moho differences in the RMS between**  
248 **an iteration and the previous one, thus showing the convergence of the algorithms (P-O**  
249 **method in blue and improved iteration P-O method in red).**

250 To illustrate the effects of the new method presented in Section 2.1, the synthetic interface  
251 of the simulation and input data were the same. In addition to the inversion method, the parameters  
252 of the calculation processes were consistent. The two methods can invert remarkably similar  
253 simulation geometries with constant density, and locations of the undulation center calculated by  
254 the improved method are very close to the original P-O method; however, our improved method  
255 calculates more accurate results. Although the iterations and time required for the calculations of  
256 our improved are longer than those of the P-O method, the center locations of bump and basin of  
257 the inversion by our method are more precise and the RMS is smaller. Figure 2 e) shows that the  
258 improved iteration P-O method can easily locate the center of fluctuation and appropriately  
259 calculate the depths. Figure 2 f) shows that the original P-O inversion method can calculate the  
260 approximate fluctuation trend, but because of the filter used in each iteration step, the specific  
261 details (the locations and depths of highlighted positions) are easily ignored and regular errors  
262 are contained in the large range of fluctuation. The iterations are shown in the Figure 3, the two  
263 methods are both convergent, and the RMS of the Moho depth differences decreases as the  
264 number of iteration increases. Moreover, although the original P-O method is faster in terms of  
265 the number of the iterations, the improved P-O method presents smaller differences in RMS.  
266 Combined with the derivation in Section 2.3, the iterative procedure of our improved method is  
267 reasonable and efficient, although it may be more complex.

268 To demonstrate the role of variable density models in the inversion of the underground  
269 interface, we changed the density contrast parameter across the interface in the previous  
270 example. Another simulation changed the density contrast model from a constant model to an  
271 exponential model. Figure 4 a) shows the same parameters of the synthetic underground interface  
272 as before and an underground interface consisting of two opposite bumps. The mean depth of  
273 interface is 27 km, the scope is 200 km×200 km, and the highest position of the interface is

274 (60,60,35), with a width of the bump of 30km. In addition, the lowest position is (120,120,17),  
 275 with a width of the depression of 40km. Figure 4 b) shows that the variable density contrast  
 276 across the interface is  $\rho = 0.5e^{-0.02h} g/cm^3$ , which is an exponential model related to the depth of  
 277 the interface. Figure 4 c) shows the gravity anomaly of the interface calculated based on Parker's  
 278 gravity forward modeling with constant-density of  $0.3g/cm^3$ , which is the average value of the  
 279 variable density contrast. Figure 4 d) shows the gravity anomaly of the interface obtained from  
 280 the Parker's gravity forward modeling with variable density, which is based on an improvement  
 281 of Parker's original study(J. FENG et al., 2014; Gao & Sun, 2019; Gómez-Ortiz & Agarwal,  
 282 2005). A carefully comparisons between Figure 4 c) and Figure 4 d) shows that the gravity  
 283 anomalies calculated by different density contrast models are different, with the results based on  
 284 Parker's gravity forward modeling with variable density usually more consistent with the actual  
 285 gravity situation. We choose the results based on variable density model of Figure 4 d) as the  
 286 input data of inversions.

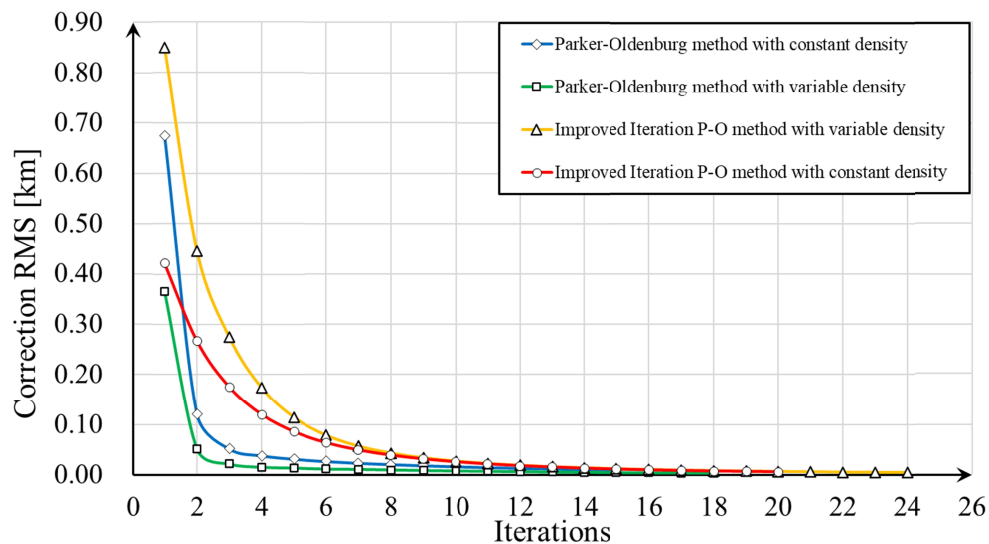


287  
 288 **Figure 4. a) Interface geometry. b) Variable density contrast modeling across the interface.**  
 289 **c) Gravity anomaly calculated by Parker's method with the constant density. d) Gravity**  
 290 **anomaly calculated by Parker's method with the variable density. e) Inversion calculated**  
 291 **by P-O method with constant density. f) Inversion calculated by P-O method with variable**  
 292 **density. g) Inversion calculated by improved iteration method with constant density. h)**  
 293 **Inversion calculated by improved iteration method with variable density. i) Difference**  
 294 **between Figure 4 a) and Figure 4 e). j) Difference between Figure 4 a) and Figure 4 f). k)**  
 295 **Difference between Figure 4 a) and Figure 4 g). l) Difference between Figure 4 a) and**  
 296 **Figure 4 h).**

297 Figure 4 e) is the inversion result of the interface calculated by the original P-O method  
 298 with the constant density contrast from the gravity anomaly, and the average density contrast is

299  $0.3g/cm^3$ . The result is that the minimum value is 15.18 km located at (118, 118), the maximum  
 300 value is 39.42 km located at (57, 57). The iterate number of the inversion is 15, the time required  
 301 for calculations is 1.78s, and the total RMS is 0.72 km. A comparison between Figure 4 e) and  
 302 Figure 4 a) is shown in Figure 4 i). Figure 4 f) shows the geometry of the inversion by the P-O  
 303 method with variable density contrast, which is calculated from the Gómez-Ortiz and Agarwal's  
 304 improved code(Gómez-Ortiz & Agarwal, 2005; ZHANG & MENG, 2013) . The exponential  
 305 model of variable density contrast is  $\rho = 0.5e^{-0.02h}g/cm^3$ . The results show that the highest point  
 306 of relief is at (58,58), with a height of 34.03km, and the lowest point of depression is at  
 307 (119,119), with a height of 18.32km. The iterate number of the inversion is 18, the time required  
 308 for calculations is 1.95s, and the total RMS compared with the simulation is 0.63 km. A  
 309 comparison between Figure 4 f) and the Figure 4 a) is shown in Figure 4 j). The comparison  
 310 between the above two results reveals that the inversion results of the P-O method using realistic  
 311 variable density parameters are better than those using approximate constant density parameters.  
 312 This conclusion has been confirmed in the previous studies.

313 Figure 4 g) shows the inversion result of the interface calculated by the improved iteration  
 314 inversion with constant density. To facilitate comparisons with previous experiment, there is no  
 315 filter in iteration process of the improved method, while the average density contrast is held  
 316 constant at  $0.3g/cm^3$ . The result is that the highest point of relief is at (57,57), with a height of  
 317 33.06km, and the lowest point of depression is at (121,121), with a height of 18.10km. The  
 318 iterate number of the inversion is 20, the time required for calculations is 1.91s, and the total  
 319 RMS compared with the simulation is 0.61 km. A comparison between Figure 4 g) and Figure 4  
 320 a) is shown in Figure 4 k). Figure 4 h) is the inversion result calculated by the improved method  
 321 with variable density contrast. The result is that the highest point of relief is at (59,59), with a  
 322 height of 34.54km, and the lowest point of depression is at (120,120), with a height of 17.50km.  
 323 The iterate number is 24, the time required for calculations is 2.21s, and the total RMS is 0.59  
 324 km. Figure 4 l) shows the Moho difference between Figure 4 a) and Figure 4 h).



325  
 326 **Figure 5. Statistics of the correction RMS, including Moho differences in the RMS between**  
 327 **an iteration and the previous one, thus showing the convergence of the algorithms (P-O**

328 **method with constant density in blue, P-O method with variable density in green, improved**  
 329 **iteration P-O method with variable density in yellow, and improved iteration P-O method**  
 330 **in red).**

331 The iterations of the four methods are shown in Figure 5, where the speed of iterative  
 332 convergence increases significantly with the addition of the variable density model; however, the  
 333 number of iterations required for convergence is also larger. The statistics in Figure 5 show that  
 334 the four methods are both stable and convergent, which is consistent with the results of previous  
 335 simulations. Based on an analysis of the simulation experiments, we found that the RMS of the  
 336 improved iteration P-O method with variable density contrast is the smallest, which means that  
 337 among the four methods, the inversion by our improved method is more precise and accurate  
 338 both in the degree and trend of inversion. However, the parameters in the iterative P-O method  
 339 with variable density are more complex, resulting in an increase in the number of iterations and  
 340 calculation time in our improved method. In addition, we find that the iterative P-O method with  
 341 variable density has some edge effects, and the application of this method in the field requires  
 342 expansion of the experimental area. Comparisons between the four methods are listed in Table 2.

343  
 344

**Table 2. The comparison between four methods in numerical experiments**

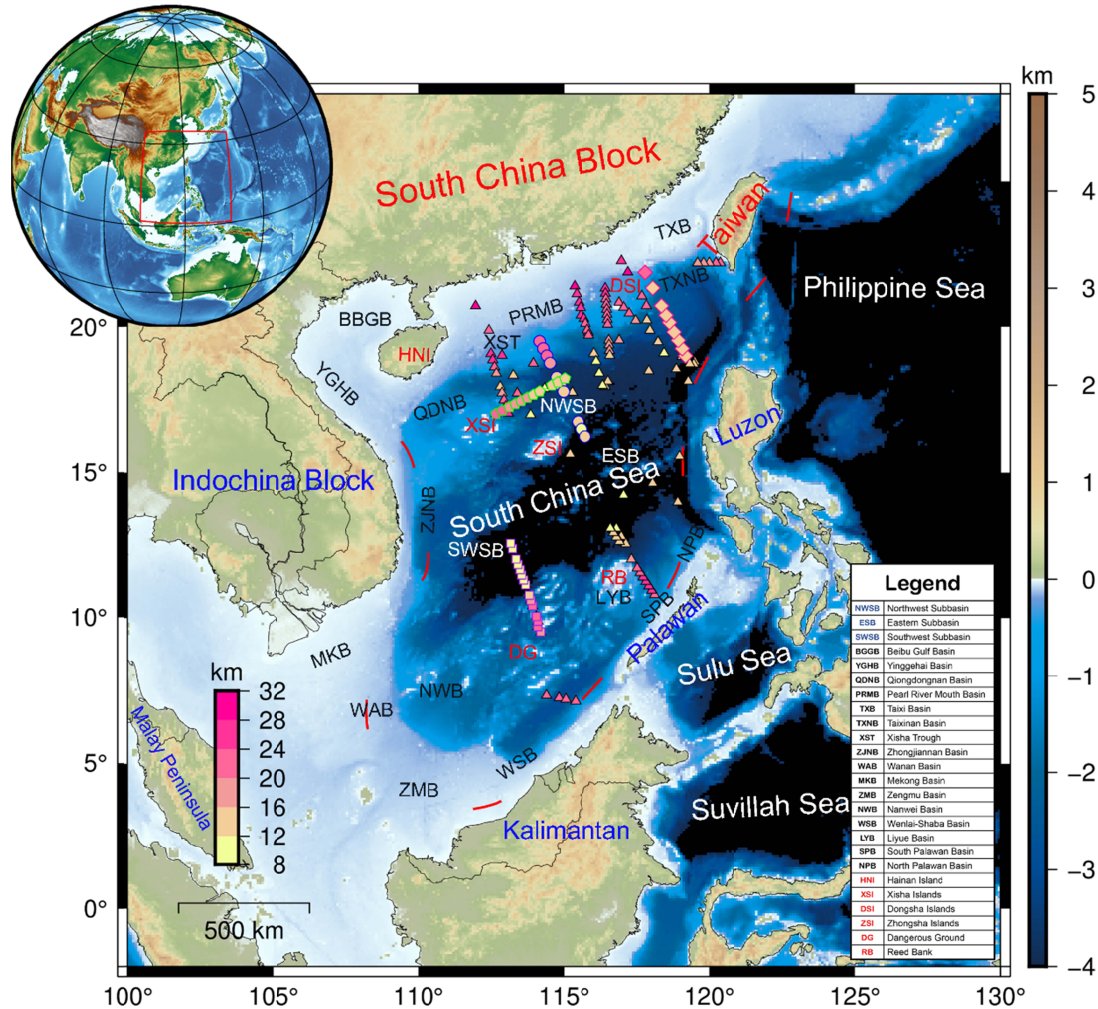
Test Groups	Contrast (g/cm <sup>3</sup> )	Highest (km)	Lowest (km)	Criterion	Iterations	Time (s)	RMS
Simulation	$\rho = 0.5e^{-0.02h}$	(60,60,35)	(120,120,17)	Null	Null	0	0
Parker-Oldenburg method (constant)	0.30	(57,57,39.42)	(118,118,15.18)	0.01	15	1.78	0.72
Parker-Oldenburg method (variable)	$\rho = 0.5e^{-0.02h}$	(58,58,34.03)	(119,119,18.32)	0.01	18	1.95	0.63
Improved Iteration P-O method (constant)	0.30	(57,57,33.06)	(121,121,18.10)	0.01	20	1.91	0.61
Improved Iteration P-O method (variable)	$\rho = 0.5e^{-0.02h}$	(59,59,34.54)	(120,120,17.50)	0.01	24	2.21	0.59

345 To investigate the improvements of the improved method, we designed four simulations with  
 346 different conditions and verified the beneficial effects of the variable density contrast parameters  
 347 on accurate inversion. In the P-O inversion method, in order to make sure the calculation was  
 348 convergent, the low-pass filter used in each iteration step, whose cutoff frequency should be  
 349 chosen carefully and tested. However, in the original P-O method, the inverted topography will  
 350 not agree with the original observations as the application of this arbitrary low-pass  
 351 filter(Oldenburg, 1974), while, a filter was not applied during the improved iteration inversion.  
 352 Compared with the synthetic model, the improved inversion method can reverse a more  
 353 reasonable result and locate a precise value in the point of dramatic change, like minimum or  
 354 maximum. In the simulation of constant density contrast, the maximum depth optimized by  
 355 56.1%, and the minimum depth improves 39.6%, in the simulation of variable density contrast,  
 356 the maximum depth optimized by 49.6%, and the minimum depth improves 62.1%. Although the  
 357 iteration in the improved inversion method are more complex than original P-O method, the  
 358 RMS of our improved inversion method is the smallest, the RMS of whole interface reduced  
 359 from 0.72 to 0.59. The above results indicate that the improved iteration P-O method with  
 360 variable density is acceptable and that the inversion is efficient and accurate.

#### 361 **4 Geophysical Example**

362 The South China Sea (SCS) located at the intersection of the Eurasian, Philippine, and Indo-  
 363 Australian Plates, which is the one of the marginal basins in the western Pacific Ocean. The

364 formation and development of the SCS were influenced by the actions of the Tethys and Pacific  
 365 tectonic domains(Hall, 2002; Taylor & Hayes, 1983). In the Cenozoic, the SCS experienced  
 366 complex evolutionary stages, including continental margin stretching, submarine expansion, and  
 367 subduction collision, and recorded the formation and evolution of the entire marginal sea. Figure  
 368 6 shows the Geological map and Moho depth seismic stations in the SCS, the small geometries  
 369 (e.g., triangles, diamonds, circles, pentagons, and squares) in Figure 6 show the positions of the  
 370 major seismic stations of the SCS.

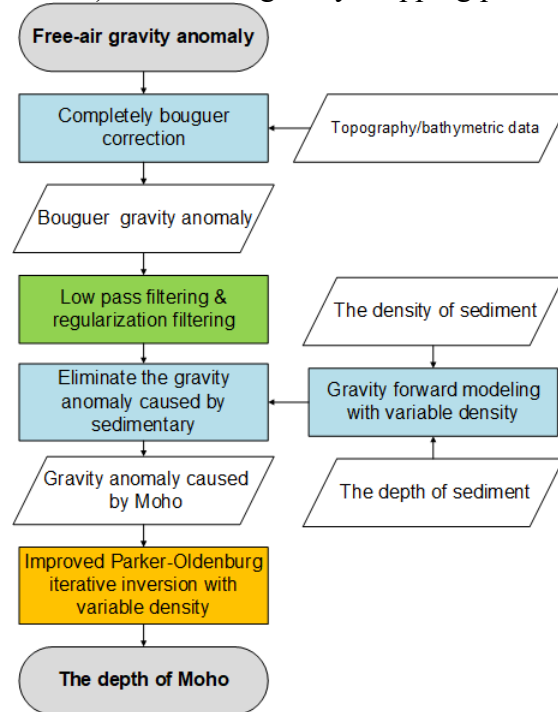


371  
 372 **Figure 6. Geological map and Moho depth seismic stations in the SCS. Colored triangles**  
 373 **with a black edge are seismic stations, which represent the traditional method of detecting**  
 374 **the depth of Moho in the SCS. Diamonds with a magenta edge represent OBS2001 (the**  
 375 **code name of ocean bottom seismograph profiles), circles with a blue edge are OBS2006-1,**  
 376 **pentagons with a green edge are OBS2006-2, squares with a purple edge are OBS2009-1.**

#### 377 4.1 The data reduction

378 We applied our improved method to a real case of the Moho inversion of the SCS, where the  
 379 research area ranges from 105°E to 122°E, and from 0°N to 26°N (separated by 5' grids). To  
 380 avoid the edge effects of the method, we chose a wider range (from 100° to 130°E and from -2° to  
 381 28°N).

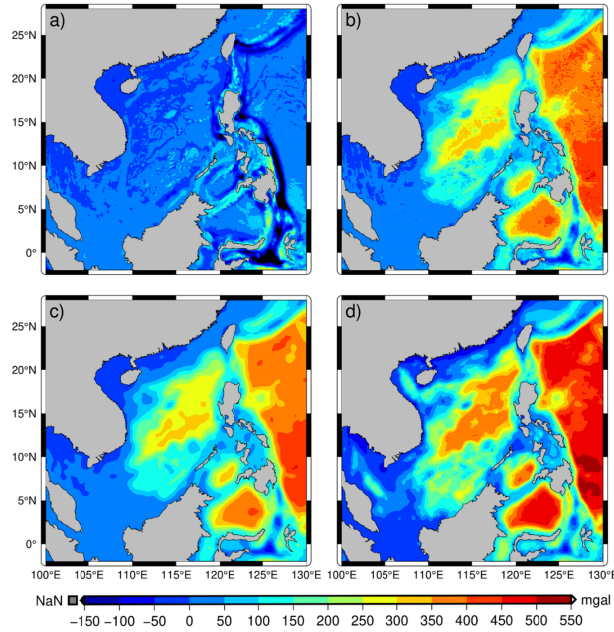
382 Among potential field methods, the target anomalous density distribution must be isolated  
 383 before modeling and inversion. In our Geophysical Example, we should reduce all gravity effects  
 384 caused by non-Moho sources signals from the original gravity observations, like topography,  
 385 sediments, mantle, etc, so that the input data of the inversion as accurate as possible. There is a  
 386 common method of data reduction is called gravity stripping: these gravitational effects caused  
 387 by other signals could be removed by accurate forward modeling of known geological models  
 388 before inversion(J. Li et al., 2022). The entire gravity stripping process is shown in Figure 7.



389  
 390

**Figure 7. The flow chart of gravity stripping.**

391 The free-air gravity anomaly of the SCS in this study was downloaded from the  
 392 International Centre for Global Earth Models (ICGEM, <http://icgem.gfz-potsdam.de/>). We chose  
 393 the latest and highest-resolution Earth's gravity field model, namely, SGG-UGM-2, from the  
 394 ICGEM. The SGG-UGM-2 model was developed by satellite gravimetry, satellite altimetry, and  
 395 Earth Gravitational Model 2008 (EGM2008)-derived gravity data(Liang et al., 2020), as  
 396 illustrated in Figure 8 a).



397  
398 **Figure 8. a) Free-air gravity anomaly of the SCS. b) Bouguer gravity anomaly of the SCS.**  
399 **c) Corrected gravity anomaly of the SCS, which eliminate the effect of mantle and deep**  
400 **Earth inhomogeneities from Bouguer gravity anomaly. d) Gravity anomaly caused by the**  
401 **Moho alone.**

402 SGG-UGM-2 ensured the validity of our original gravity data in our case region of the SCS,  
403 as SGG-UGM-2 had the new marine gravity anomalies and the contribution of the new GRACE  
404 normal equation. First, the gravity anomaly reduced the gravity effects of topography (Rexer et  
405 al., 2016), and the bouguer correction of SGG-UGM-2 from free-air anomaly to Bouguer gravity  
406 anomaly was conducted on a global scale. This correction is better than the small regional  
407 bouguer correction that was previously applied. Global topographic data were downloaded from  
408 NOAA(National Oceanic and Atmospheric Administration,  
409 <https://www.ngdc.noaa.gov/mgg/global/global.html>) and SIO (Scripps Institution of  
410 Oceanography, <http://topex.ucsd.edu/>). The Bouguer gravity anomaly is shown in Figures 8 b).  
411 Second, the Bouguer gravity anomaly eliminated the effect of mantle and deep Earth  
412 inhomogeneities, which were stripped from degree 1 to 17 spherical harmonics (Bagherbandi &  
413 Sjöberg, 2012; Jiménez-Munt et al., 2008; Kumar et al., 2013), as shown in Figure 8 c).

414 Finally, the gravitational attraction of these huge marine sediments cannot be ignored, we  
415 should eliminate the gravity anomaly caused by sedimentation, which can be calculated using  
416 tesseroids(Lin et al., 2020). We obtained the data of sediment thickness from the NOAA  
417 (<https://www.ngdc.noaa.gov/mgg/sedthick/index.html>). The sediment depth-density function of  
418 the SCS can be fitted using seismic and borehole sample data(M. Chen et al., 2018). The  
419 function is expressed as follows:

$$420 \quad \rho_z = \phi_0 e^{-cz} \rho_w + (1 - \phi_0 e^{-cz}) \rho_{sg} \quad (12)$$

421 where  $\rho_z$  presents the density differences of sediment layers,  $Z$  is the thickness of sediment  
422 layers,  $c$  is the conversion parameters,  $\rho_w$  means the density of seawater, and  $\rho_{sg}$  means the  
423 density of filled granules.  $\phi_0, \rho_{sg}, c$  can be calculated by the wave velocity-density conversion  
424 equation based on the P-wave velocity of the seabed seismograph sounding profile. Thus, the

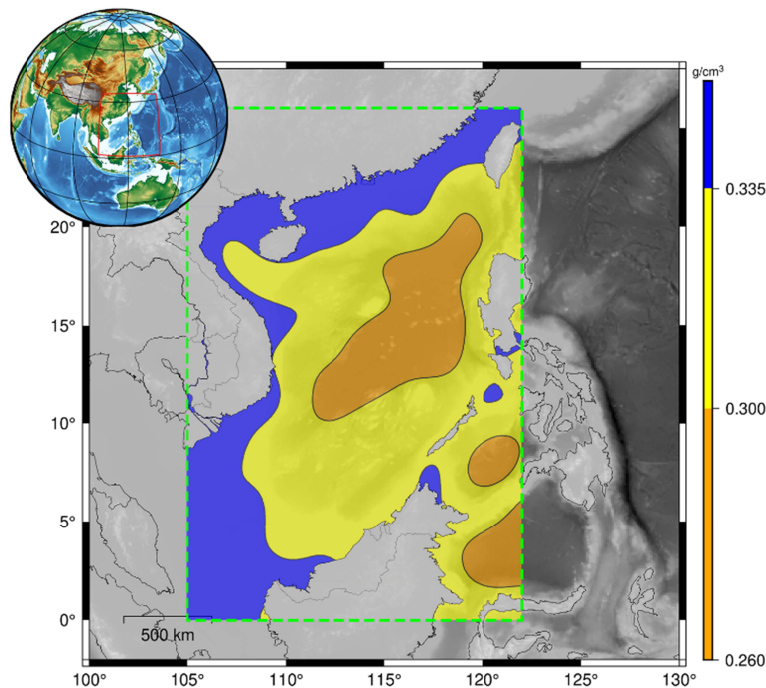
425 Bouguer gravity anomaly after removing the gravity effects of sediments, the mantle and deep  
 426 Earth inhomogeneities is called gravity anomaly caused by Moho (Figure 8 d)), which is  
 427 associated only with Moho relief and we can use it in the Moho inversion.

## 428 4.2 Results and Discussions

429 We derived the formulas for the improved iterative inversion with variable density, and  
 430 demonstrated the efficacy of our method though a series of simulations in the above section.  
 431 Here, we apply our improved method to a real case of a Moho inversion of the SCS, where the  
 432 area range of research has been mentioned in Section 4.1.

433 After gravity stripping, the gravity anomaly caused by the Moho is shown in Figure 8 d),  
 434 and the mean Moho depth ( $z_0 = 24.63 \text{ km}$ ) is estimated from seismic Moho depth control points  
 435 (colored geometries in Figure 6)(Hung et al., 2021; Wei et al., 2020), which can also be applied  
 436 as a reference for comparison between the Moho models and seismic measurements obtained  
 437 from previous geological studies of the SCS.

438 With our improved method, the parameter of density contrast in the reality is variable, that  
 439 cannot be ignored. Owing to the lack of accurate density information, we must choose a safer  
 440 and more widely recognized indicator to estimate the lateral variation in the SCS Moho density  
 441 contrast. With contemporaneous stratigraphic densities varying considerably from region to  
 442 region, obvious lateral density zoning features occur in the SCS(J. Chen et al., 2012).As shown  
 443 in the Figure 6, the study area can be roughly divided into three crustal types crusts according to  
 444 the submarine topography in geology: oceanic crusts, continental-oceanic transitional crusts, and  
 445 thinning continental crusts. Based on the seismic profile data and Bouguer gravity anomaly data  
 446 in the SCS, the densities of the sediment layer, basement layer, and upper crust can be estimated  
 447 by using the empirical formula for wave velocity-density conversion. Finally, we obtained a  
 448 variable density contrast model for the SCS (Figure 9) with an attenuation coefficient of 0.002.



449 **Figure 9. Variable density contrast model in the SCS.**  
 450

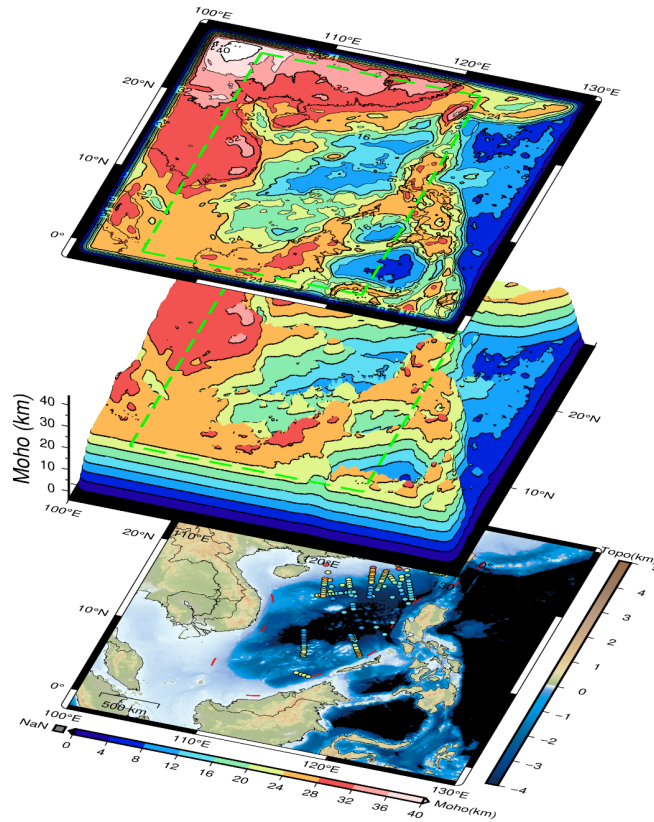


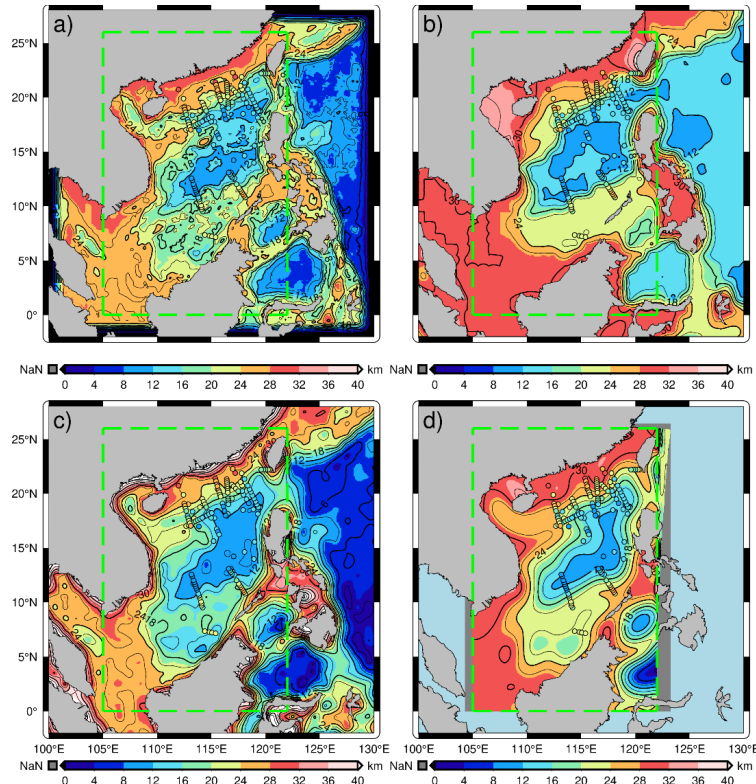
**Figure 10 Composite image of the Moho inversion in the South China Sea.**

Using the variable density contrast model, the mean depth of Moho, and gravity anomaly caused by Moho (Figure 8 d)), the SCS Moho depth model could be calculated precisely by our improve iteration P-O method with variable density(Figure 10). Figure 10 is a composite image of the Moho depths model in the SCS, which includes three layers. The lower layer is the topographic map of the SCS, as shown in the simplified version of Figure 6, where the colored dots in the lower image indicate the seismic stations in the SCS, and the depths of the Moho surface from the seismic data in the SCS are shown by the color of those dots. The middle layer is a three-dimensional image of our Moho depths model in the SCS, and the green dashed line frames the effective scope of the model, which ranges from 105°E to 122°E, and 0°N to 26°N and has a resolution of 5'. The upper layer is the Moho depth contour map at intervals of 4 km.

Figure 10 shows that the SCS Moho depth model exhibits distinct zoning, and consists of divisions of the three crustal types. The model showed that the Moho depths were approximately 7-14 km in the sea basin area (e.g., South China Sea, Sulu Sea, Suvillah Sea, and Philippine Sea), and the Moho surface depths in continental crust area are more than 25 km (e.g., the South China Block, Indo-China Block, northwestern continental shelves, and Luzon Island). The Ocean-land transitional crust occurs between the continental crust and oceanic crusts, the depth of the Moho in the SCS is about 14-25 km, and the Moho model of the SCS has an obvious regional characteristic. Large undulations occur in the area of continental-oceanic transitional crusts, which reflects the uplift of the Moho and the upwelling of the upper mantle in the lower part of the sea basin. This upwelling provided heat source for the YingGehai Basin, ZengMu Basin, and other oil and gas resource-producing areas in the continental-oceanic transitional areas.

To better understand the Moho depth model of our improved method, we examined the differences between our results and previous modeling results, as shown in Figure 11 and Table

476 3. To focus on the features of Moho depths in the ocean parts of the SCS, the land areas of all the  
 477 Moho depths models are shown in Figure 11. Figure 11 a) shows our Moho depth model, which  
 478 is inverted by the improved iteration P-O method with variable density, and it is consistent with  
 479 the upper image of Figure 10. We will not repeat the characteristics of our Moho depth model  
 480 here.



481 **Figure 11. a) The Moho depth model calculated by improved iteration Parker-Oldenburg**  
 482 **method with variable density (the circles mean the seismological data in the SCS). b) The**  
 483 **CRUST1.0. c) The Moho depth model calculated by global P-O method, which is defined**  
 484 **under a spherical coordinate system. d) The Moho depth model by original P-O method**  
 485 **with variable Moho density contrast.**

487 Figure 11 b) shows the depth of the Moho from CRUST1.0 in the SCS(Laske et al., 2013).  
 488 CRUST1.0 is an updated global model of Earth's crustal structure based on a new database of  
 489 crustal thickness data from active source seismic studies as well as from receiver function  
 490 studies, which is defined on a 1-degree grid. Figure 11 b) and Figure 11 a) show that the Moho  
 491 depths obtained from CRUST1.0 are deeper than that of our depth model for the thinning  
 492 continental crust but shallower than that of our model in the sea basin area. In areas with thick  
 493 sediment layers, such as the Yinggehai Basin, Pear River Mouth Basin, and Nanwei Basin, clear  
 494 differences are observed between the Moho depths from the CRUST1.0 model and our improved  
 495 model. Previous studies have shown that there are some differences between the Airy and  
 496 gravimetric Moho models, which can not be overlooked and these differences are associated with  
 497 unconsidered sediment loads and various isostatic assumptions(Eshagh, 2020).

498 Figure 11 c) shows the Moho inversion of the SCS based on the global P-O method, which is  
 499 defined under a spherical coordinate system (Chen's global Moho model for short)(W. Chen &  
 500 Tenzer, 2020). A large-scale region of Chen's global Moho model confirms that the results of  
 501 gravimetric forward modelling and inversion will be improved after a global integration and by

502 considering Earth's sphericity. Figure 11 c) and Figure 11 a) show that Chen's global Moho  
 503 model is closely associated with our Moho depth model in terms of the general distributions of  
 504 the SCS, although Chen's global Moho model generates deeper Moho depths in the oceanic  
 505 crusts compared with our Moho model.

506 Figure 11 d) shows the Moho depths derived by an iterative inversion in the spatial  
 507 domain (Zhang's Moho model for short)(ZHANG et al., 2020), which is constrained by the  
 508 requirement of known depth information. Zhang's Moho model introduces a horizontal density  
 509 partition and reduces the systematic error by evaluating the accuracy of the constraint. Figure 11  
 510 a), Figure 11 b) and Figure 11 c) show that the depths of Zhang's Moho model are greater than  
 511 that of the other models and the undulations of the Moho depth are smooth, which may be related  
 512 to the difference between the inversion method of the spatial and frequency domain.

513 Table 3 shows the statistics on the comparisons between these Moho depths models and  
 514 seismological data. The Moho differences between our Moho model and seismological data  
 515 range from -5.53 km to 8.40 km, and the RMS of the difference is 3.87 km, which is the smallest  
 516 among the investigated models. The comparison of Figure 11 and Table 3 show that our Moho  
 517 depth model calculated using the improved iteration P-O method with variable density presents  
 518 the most accurate result.

519 Table 3 Comparison of different Moho models at the positions of seismic stations in the SCS.

Name	Max (km)	Min (km)	Mean (km)	RMS (km)	Reference
CRUST1.0 Moho depth model	11.55	-8.90	0.41	4.92	(Laske et al., 2013)
Global P-O method defined for a spherical coordinate system	7.17	-8.22	-1.10	13.75	(W. Chen & Tenzer, 2020)
Improved iteration P-O method with variable Moho density contrast	<b>8.40</b>	<b>-5.53</b>	<b>0.19</b>	<b>3.87</b>	The paper
Iterative inversion in spatial domain under the constraint of known depth information.	11.63	-3.09	2.50	24.12	(ZHANG et al., 2020)

520

## 521 5 Conclusions

522 In study, we deduced the original Parker-Oldenburg method, which is a widely used interface  
 523 inversion method in the frequency domain. Based on the Xu's theory, we proposed an improved  
 524 iteration P-O method with variable density. The effectiveness of our improved method was  
 525 validated using both synthetic experiments and the geophysical examples.

526 In the synthetic experiments, we designed a numerical experiment to analyze the effect of  
 527 our improved iterative algorithm. The results show that our improved method can easily locate  
 528 the center of fluctuation and reasonably calculate the depths of the interface, the RMS of our  
 529 method is smaller than that of the original P-O method. Furthermore, we designed another  
 530 simulation to demonstrate the role of variable density models in the inversion of the underground  
 531 interface and compared our improved method with the original P-O method based on the variable

532 density model. The results show that the RMS of our improved method with variable density is  
533 the smallest; however, the calculation process is complex because of the parameters of the  
534 variable density are inconsistent.

535 In the real case, we adapted our improved inversion method to calculate the Moho depths of  
536 the SCS. The gravity anomaly caused by the Moho was derived from the global gravity field  
537 model SGG-UGM-2. During gravity stripping, the lower degree/order term of global gravity  
538 field model is subtracted to eliminate the effect of mantle and deep-earth inhomogeneities. The  
539 free-air gravity anomaly of SGG-UGM-2 reduced the gravity effects of topography and  
540 sediment. The mean Moho depth of the SCS (24.63km) was averaged from the depths of all the  
541 seismic Moho depth stations. Based on the empirical formula for the wave velocity-density  
542 conversion, we obtained a variable density contrast model with an attenuation coefficient of  
543 0.002. The Moho depth model inverted by our improved method shows that the Moho depths of  
544 the SCS have an obvious regional characteristic, the depths in the sea basin area are  
545 approximately 7-14 km, and the Moho surface depths in the continental crust area are more than  
546 25 km. Ocean-land transitional crust occurs between the continental and oceanic crusts, and the  
547 depths of the Moho surface in this area are approximately 14-25 km.

548 Last, we examine the differences between our Moho model and previous models and  
549 compare the effects of the Moho depth models to real ocean bottom seismograph profiles in the  
550 SCS. The RMS of the difference between our Moho model and the seismological data is the  
551 smallest of 3.87km, and our Moho model also shows accurate Moho depths at the checkpoints,  
552 which means that our improved method is efficient and practical. The results of the synthetic  
553 experiments and the geophysical examples are as follows:

- 554 1. The improved Parker-Oldenburg method used an upward continuation form in the Fourier  
555 domain in the iteration processing, and finally the algorithm can obtain convergent inversion  
556 results.
- 557 2. Filters or any regularization factors are not included in the iteration processing of our  
558 improved method, which results in fewer empirical parameters in the calculation and more  
559 detailed information.
- 560 3. Owing to the constraints of gravity data and geological information, the results of our  
561 improved method with variable density correspond well with reality.

562 This study provides an improved method of inverting Moho depths from gravity anomalies,  
563 although improvements remain to be made in the future. The mean depth of the interface can be  
564 estimated from scientific methods instead of actual data, and if the variable Moho density model  
565 can be obtained accurately from the geological approach, then we believe that the more exciting  
566 results can be achieved.

## 567 **Data Availability Statement**

568 Data sets for this research are available from the NOAA(National Oceanic and Atmospheric  
569 Administration, <https://www.ngdc.noaa.gov/mgg/global/global.html>) and SIO (Scripps  
570 Institution of Oceanography, <http://topex.ucsd.edu/>), and the International Centre for Global  
571 Earth Models (ICGEM, <http://icgem.gfz-potsdam.de/>), respectively.

## 572 **Acknowledgments**

573 The research is supported by the Open Fund of Hubei LuoJia Laboratory (grant no.  
574 220100057), the National Natural Science Foundation of China (grant no. 42104024), the

575 Fundamental Research Funds for the Central Universities, China University of Geosciences  
 576 (Wuhan) (grant no. CUGL200805), and the Open Fund of Wuhan Gravitation and Solid Earth  
 577 Tides, National Observation and Research Station (WHYWZ202115).

## 578 References

- 579 Agius, M. R., & Lebedev, S. (2014). Shear-velocity structure, radial anisotropy and dynamics of the Tibetan crust.  
 580 *Geophysical Journal International*, 199(3), 1395-1415.
- 581 Ahmed, N., Natarajan, T., & Rao, K. R. (1974). Discrete cosine transform. *IEEE transactions on Computers*, 100(1),  
 582 90-93.
- 583 Bagherbandi, M. (2012). A comparison of three gravity inversion methods for crustal thickness modelling in Tibet  
 584 plateau. *Journal of Asian Earth Sciences*, 43(1), 89-97.
- 585 Bagherbandi, M., & Sjöberg, L. E. (2012). Non-isostatic effects on crustal thickness: a study using CRUST2. 0 in  
 586 Fennoscandia. *Physics of the Earth and Planetary Interiors*, 200, 37-44.
- 587 Bott, M. (1960). The use of rapid digital computing methods for direct gravity interpretation of sedimentary basins.  
 588 *Geophysical Journal International*, 3(1), 63-67.
- 589 Chai, Y., & Jia, J. (1990). Parker's formulas in different forms and their applications to oil gravity survey. *Oil*  
 590 *Geophysical Prospecting*, 25, 321-332.
- 591 Chappell, A., & Kusznir, N. (2008). An algorithm to calculate the gravity anomaly of sedimentary basins with  
 592 exponential density - depth relationships. *Geophysical Prospecting*, 56(2), 249-258.
- 593 Chen, J., Zhu, B.-D., Wen, N., & Wan, R.-S. (2012). Gravity-magnetic response of the islands and seamounts of  
 594 South China Sea. *Chinese Journal of Geophysics*, 55(09), 3152-3162.
- 595 Chen, M., Fang, J., & Cui, R. (2018). Lithospheric structure of the South China Sea and adjacent regions: Results  
 596 from potential field modelling. *Tectonophysics*, 726, 62-72.
- 597 Chen, Q., Shen, Y., Francis, O., Chen, W., Zhang, X., & Hsu, H. (2018). Tongji - Grace02s and Tongji - Grace02k:  
 598 high - precision static GRACE - only global Earth's gravity field models derived by refined data  
 599 processing strategies. *Journal of geophysical research: solid earth*, 123(7), 6111-6137.
- 600 Chen, W., & Tenzer, R. (2017). Moho modeling in spatial domain: A case study under Tibet. *Advances in Space*  
 601 *Research*, 59(12), 2855-2869.
- 602 Chen, W., & Tenzer, R. (2020). Reformulation of Parker-Oldenburg's method for Earth's spherical approximation.  
 603 *Geophysical Journal International*, 222(2), 1046-1073.
- 604 Drinkwater, M., Floberghagen, R., Haagmans, R., Muzi, D., & Popescu, A. (2003). VII: Closing session: GOCE:  
 605 ESA's first earth explorer core mission. *Space science reviews*, 108(1), 419-432.
- 606 DU, W., DONG, J., CHEN, X., ZHANG, Y., LIU, J., & HUI, M. (2022). Calculation of Curie depth in Qinghai  
 607 Province based on an improved Parker-Oldenburg interface inversion method. *Chinese Journal of*  
 608 *Geophysics*, 65(3), 1096-1106.
- 609 Eshagh, M. (2020). *Satellite Gravimetry and the Solid Earth: Mathematical Foundations*: Elsevier.
- 610 FENG, J., MENG, X.-H., CHEN, Z.-X., SHI, L., WU, Y., & FAN, Z.-J. (2014). The investigation and application of  
 611 three-dimensional density interface. *Chinese Journal of Geophysics*, 57(1), 287-294.
- 612 Feng, R., YAN, H.-F., & ZHANG, R.-S. (1986). The rapid inversion of 3-D potential-field and program design.  
 613 *Acta Geologica Sinica*, 60(4), 390-403.
- 614 Gao, X., & Sun, S. (2019). Comment on "3DINVER. M: A MATLAB program to invert the gravity anomaly over a  
 615 3D horizontal density interface by Parker-Oldenburg's algorithm". *Computers and Geosciences*, 127, 133-  
 616 137.
- 617 Gómez-Ortiz, D., & Agarwal, B. N. (2005). 3DINVER. M: a MATLAB program to invert the gravity anomaly over  
 618 a 3D horizontal density interface by Parker-Oldenburg's algorithm. *Computers & geosciences*, 31(4), 513-  
 619 520.
- 620 Granser, H. (1987). Three - dimensional interpretation of gravity data from sedimentary basins using an exponential  
 621 density - depth function. *Geophysical Prospecting*, 35(9), 1030-1041.
- 622 Grigoriadis, V. N., Tziavos, I. N., Tsokas, G. N., & Stampolidis, A. (2016). Gravity data inversion for Moho depth  
 623 modeling in the Hellenic area. *Pure and Applied Geophysics*, 173(4), 1223-1241.
- 624 Guan, X. (1991). An effective and simple approach of subsurface inversion using Parker's equation. *Computing*  
 625 *Techniques for Geophysical and Geochemical Exploration*, 13(3), 236-242.

- 626 Guspi, F. (1992). Three-dimensional Fourier gravity inversion with arbitrary density contrast. *Geophysics*, 57(1),  
627 131-135.
- 628 Hall, R. (2002). Cenozoic geological and plate tectonic evolution of SE Asia and the SW Pacific: computer-based  
629 reconstructions, model and animations. *Journal of Asian Earth Sciences*, 20(4), 353-431.
- 630 HE, H., FANG, J., CHEN, M., & CUI, R. (2019). Moho Depth of the East China Sea Inversed Using Gravity Data.  
631 *Geomatics and Information Science of Wuhan University*, 44(5), 682-689.
- 632 Hung, T. D., Yang, T., Le, B. M., Yu, Y., Xue, M., Liu, B., et al. (2021). Crustal Structure Across the Extinct Mid -  
633 Ocean Ridge in South China Sea From OBS Receiver Functions: Insights Into the Spreading Rate and  
634 Magma Supply Prior to the Ridge Cessation. *Geophysical Research Letters*, 48(3), e2020GL089755.
- 635 Jiménez-Munt, I., Fernández, M., Vergés, J., & Platt, J. P. (2008). Lithosphere structure underneath the Tibetan  
636 Plateau inferred from elevation, gravity and geoid anomalies. *Earth and Planetary Science Letters*, 267(1-  
637 2), 276-289.
- 638 KE, X., WANG, Y., & XU, H. (2006). Moho depths inversion of Qinghai-Tibet plateau with variable density model.  
639 *Geomatics and Information Science of Wuhan University*, 31(4), 289-292.
- 640 Koulakov, I., Maksotova, G., Mukhopadhyay, S., Raof, J., Kayal, J., Jakovlev, A., & Vasilevsky, A. (2015).  
641 Variations of the crustal thickness in Nepal Himalayas based on tomographic inversion of regional  
642 earthquake data. *Solid Earth*, 6(1), 207-216.
- 643 Kumar, N., Zeyen, H., Singh, A., & Singh, B. (2013). Lithospheric structure of southern Indian shield and adjoining  
644 oceans: integrated modelling of topography, gravity, geoid and heat flow data. *Geophysical Journal  
645 International*, 194(1), 30-44.
- 646 Kvas, A., Brockmann, J. M., Krauss, S., Schubert, T., Gruber, T., Meyer, U., et al. (2021). GOCO06s—a satellite-  
647 only global gravity field model. *Earth System Science Data*, 13(1), 99-118.
- 648 Laske, G., Masters, G., Ma, Z., & Pasyanos, M. (2013). *Update on CRUST1. 0—A 1-degree global model of Earth's  
649 crust*. Paper presented at the Geophysical research abstracts.
- 650 LI, H., WU, Z., JI, F., GAO, J., YANG, C., Yuan, Y., et al. (2020). Crustal density structure of the northern South  
651 China Sea from constrained 3-D gravity inversion. *Chinese Journal of Geophysics*, 63(5), 1894-1912.
- 652 Li, J., Xu, C., & Chen, H. (2022). An improved method to Moho depth recovery from gravity disturbance and its  
653 application in the South China Sea. *Journal of geophysical research: solid earth*, 127(7), e2022JB024536.
- 654 Liang, W., Li, J., Xu, X., Zhang, S., & Zhao, Y. (2020). A high-resolution Earth's gravity field model SGG-UGM-2  
655 from GOCE, GRACE, satellite altimetry, and EGM2008. *Engineering*, 6(8), 860-878.
- 656 Lin, M., Denker, H., & Müller, J. (2020). Gravity field modeling using tesseroids with variable density in the  
657 vertical direction. *Surveys in Geophysics*, 41(4), 723-765.
- 658 Luo, Y., & Wu, M. P. (2016). Minimum curvature method for downward continuation of potential field data.  
659 *Chinese Journal of Geophysics-Chinese Edition*, 59(1), 240-251. <Go to ISI>://WOS:000368048800020
- 660 Nagendra, R., Prasad, P., & Bhimasankaram, V. (1996). Forward and inverse computer modeling of a gravity field  
661 resulting from a density interface using Parker-Oldenberg method. *Computers & geosciences*, 22(3), 227-  
662 237.
- 663 Obrebski, M., Allen, R. M., Zhang, F., Pan, J., Wu, Q., & Hung, S. H. (2012). Shear wave tomography of China  
664 using joint inversion of body and surface wave constraints. *Journal of geophysical research: solid earth*,  
665 117(B1).
- 666 Oldenburg, D. W. (1974). The inversion and interpretation of gravity anomalies. *Geophysics*, 39(4), 526-536.
- 667 Parker, R. (1973). The rapid calculation of potential anomalies. *Geophysical Journal International*, 31(4), 447-455.
- 668 Pavlis, N. K., Holmes, S. A., Kenyon, S. C., & Factor, J. K. (2012). The development and evaluation of the Earth  
669 Gravitational Model 2008 (EGM2008). *Journal of geophysical research: solid earth*, 117(B4).
- 670 Qin, P., Zhang, C., Meng, Z., Zhang, D., & Hou, Z. (2021). Three Integrating Methods for Gravity and Gravity  
671 Gradient 3-D Inversion and Their Comparison Based on a New Function of Discrete Stability. *IEEE  
672 Transactions on Geoscience and Remote Sensing*.
- 673 Reigber, C., Lühr, H., & Schwintzer, P. (2002). CHAMP mission status. *Advances in Space Research*, 30(2), 129-  
674 134.
- 675 Rexer, M., Hirt, C., Claessens, S., & Tenzer, R. (2016). Layer-based modelling of the Earth's gravitational potential  
676 up to 10-km scale in spherical harmonics in spherical and ellipsoidal approximation. *Surveys in  
677 Geophysics*, 37(6), 1035-1074.
- 678 Shi, L., Li, Y., & Zhang, E. (2015). A new approach for density contrast interface inversion based on the parabolic  
679 density function in the frequency domain. *Journal of Applied Geophysics*, 116, 1-9.
- 680 Shin, Y. H., Choi, K. S., & Xu, H. (2006). Three-dimensional forward and inverse models for gravity fields based  
681 on the Fast Fourier Transform. *Computers & geosciences*, 32(6), 727-738.

- 682 Sjöberg, L. E. (2009). Solving Vening Meinesz-Moritz inverse problem in isostasy. *Geophysical Journal*  
683 *International*, 179(3), 1527-1536.
- 684 Sjöberg, L. E. (2013). On the isostatic gravity anomaly and disturbance and their applications to Vening Meinesz-  
685 Moritz gravimetric inverse problem. *Geophysical Journal International*, 193(3), 1277-1282.
- 686 Tapley, B. D., Bettadpur, S., Ries, J. C., Thompson, P. F., & Watkins, M. M. (2004). GRACE measurements of  
687 mass variability in the Earth system. *science*, 305(5683), 503-505.
- 688 Taylor, B., & Hayes, D. E. (1983). Origin and History of the South China Sea Basin. *The Tectonic and Geologic*  
689 *Evolution of Southeast Asian Seas and Islands: Part 2*, 27, 23-56.
- 690 Teng, J., Zhang, Z., Zhang, X., Wang, C., Gao, R., Yang, B., et al. (2013). Investigation of the Moho discontinuity  
691 beneath the Chinese mainland using deep seismic sounding profiles. *Tectonophysics*, 609, 202-216.
- 692 Wang, Q., Hawkesworth, C. J., Wyman, D., Chung, S.-L., Wu, F.-Y., Li, X.-H., et al. (2016). Pliocene-Quaternary  
693 crustal melting in central and northern Tibet and insights into crustal flow. *Nature Communications*, 7(1),  
694 1-11.
- 695 Wang, X., Li, Y., Ding, Z., Zhu, L., Wang, C., Bao, X., & Wu, Y. (2017). Three - dimensional lithospheric S wave  
696 velocity model of the NE Tibetan Plateau and western North China Craton. *Journal of geophysical*  
697 *research: solid earth*, 122(8), 6703-6720.
- 698 Wei, X., Ruan, A., Ding, W., Wu, Z., Dong, C., Zhao, Y., et al. (2020). Crustal structure and variation in the  
699 southwest continental margin of the South China Sea: Evidence from a wide-angle seismic profile. *Journal*  
700 *of Asian Earth Sciences*, 203, 104557.
- 701 Xia, J., & Sprowl, D. R. (1995). Moho depths in Kansas from gravity inversion assuming exponential density  
702 contrast. *Computers & geosciences*, 21(2), 237-244.
- 703 XIAO, P.-f., CHEN, S.-c., MENG, L.-s., & YANG, J.-y. (2007). The density interface inversion of high-precision  
704 gravity data. *Geophysical and Geochemical Exploration*(1), 29-33.
- 705 XU, S. Z. (2006). The integral - iteration method for continuation of potential fields. *Chinese Journal of*  
706 *Geophysics*, 49(4), 1054-1060.
- 707 Zeng, H., Zhang, Q., Li, Y., & Liu, J. (1997). Crustal structure inferred from gravity anomalies in South China.  
708 *Tectonophysics*, 283(1-4), 189-203.
- 709 Zeng, X. N., Li, X. H., Su, J., Liu, D. Z., & Zou, H. X. (2013). An adaptive iterative method for downward  
710 continuation of potential-field data from a horizontal plane. *Geophysics*, 78(4), J43-J52. <Go to  
711 ISI>://WOS:000322716500029
- 712 Zhang, C., Huang, D., Wu, G., Ma, G., Yuan, Y., & Yu, P. (2015). Calculation of moho depth by gravity anomalies  
713 in Qinghai-Tibet plateau based on an improved iteration of Parker-Oldenburg inversion. *Pure and Applied*  
714 *Geophysics*, 172(10), 2657-2668.
- 715 ZHANG, E.-H., SHI, L., LI, Y.-H., WANG, Q.-S., & HAN, C.-W. (2015). 3D interface inversion of gravity data in  
716 the frequency domain using a parabolic density-depth function and the application in Sichuan-Yunnan  
717 region. *Chinese Journal of Geophysics*, 58(2), 556-565.
- 718 ZHANG, S., & MENG, X.-h. (2013). Constraint interface inversion with variable density model. *Progress in*  
719 *Geophysics*, 28(4), 1714-1720.
- 720 ZHANG, S., ZHANG, M., LIU, L., QIAO, J., & LIU, S. (2020). Improved interface inversion based on constrained  
721 varying density and its application. *Chinese Journal of Geophysics*, 63(10), 3886-3895.
- 722 Zhou, X. (2009). 3D vector gravity potential and line integrals for the gravity anomaly of a rectangular prism with  
723 3D variable density contrast. *Geophysics*, 74(6), I43-I53.
- 724